Homogeneous and heterogeneous rheology and flow-induced microstructures of a fresh fiber-reinforced mortar

F. Chalencon [a,b,c], P.J.J. Dumont [d,*], L. Orgéas [a,b], G. Foray [c], J.-Y. Cavaillé [c], E. Maire [c]

[a] 3SR Lab, Univ. Grenoble Alpes, F-38000 Grenoble, France
[b] 3SR Lab, CNRS, F-38000 Grenoble, France
[c] MATEIS CNRS UMR5510, INSA-Lyon, Université de Lyon, F-69621 Villeurbanne, cedex, France
[d] LaMCoS CNRS UMR5259, INSA-Lyon, Université de Lyon, F-69621 Villeurbanne, cedex, France

ARTICLE INFO

ABSTRACT

External wall insulation (EWI) usually comprises a porous cement mortar used as protective external render into which short fibers are added to enhance its mechanical properties. The rheology of these porous, fibrous, and granular suspensions was investigated using lubricated compression tests in the fresh state, whereas flow-induced porous microstructures were studied using X-ray microtomography. We show that these suspensions exhibit a homogeneous isovolume flow regime and two heterogeneous flow regimes, *i.e.*, a consolidating regime, and a consolidating and segregating regime. A decrease in the compression strain rate and/or an increase in the number of fiber contacts in the entangled fibrous network induced flow heterogeneity accompanied by heterogeneous modifications of density, porosity, and pore size distribution of render. These undesirable microstructure changes are prone to occur during mortar processing and placement. They drastically affect the properties of renders such as the permeability that was calculated using X-ray microtomography images and pore scale numerical simulation.

1. Introduction

External wall insulation (EWI) is an interesting technology for the thermal insulation of buildings. EWI limits thermal bridges compared to other insulation systems and can be used for aesthetic purposes. An EWI system generally comprises an insulating layer made up of polystyrene, polyurethane, wood, or mineral wool topped off with a protective render, *i.e.*, a highly porous cement mortar reinforced with glass or metal fiber meshes. The placement of the render involves at least four operations. A first layer of render is sprayed onto the insulating material. Then a glass fiber mesh is fixed in the wet render and a second layer of render is added. Finally, a third layer of finishing render is placed after one or two weeks. The cost induced by these numerous processing operations hinders the development of this insulation technique. However, the use of renders that are self-reinforced with discontinuous fibers constitutes an interesting alternative to the classical EWI systems [1]. Self-reinforced renders are sprayed onto the insulation material in one operation using specially designed apparatuses. Hence, these renders must exhibit a particular and complex rheological behavior, which leads to complicated formulation problems. Indeed, they have to undergo flow as they are conveyed through the pneumatic spraying apparatus, projected onto the insulation materials, and levelled. They must

also stick onto the insulating material without flowing. Thus, during these stages, where fresh mortars are subjected to a wide range of strain rates (from very low to very high values), it is of great importance to control their flow-induced granular, fibrous, and porous microstructures. Such evolution of render structures drastically affect the mechanical and physical properties of mortars in their hardened state [15,16], such as their permeability, which plays an important role for the performance of the EWI systems.

Characterizing and controlling the rheology of these fiber-reinforced and porous renders is a complex problem. For instance, it is well known that adding fibers into fresh cements induces important variations in their rheological behavior, with complex thickening effects, evolution of fiber orientation and placement [2–9,57] that modify their microstructure [4,8,9,13,14]. The study of the links between the evolution of the microstructure of self-reinforced renders and the processing conditions involves the use of suitable experimental devices. In a previous study [17], lubricated compression experiments were performed using a rheometer having large dimensions. For these tests, a commercial organo-mineral render (ParexLanko, Maité monocomposant) was reinforced with commercial alkali-resistant glass fiber bundles (Owens Corning, Cemfil Anti-crack). Two types of fiber bundles were also used, *i.e.*, high performance (HP) or highly dispersive (HD) fiber bundles, with fiber contents and aspect ratios typically used for practical applications. Coupled with an analysis of the microstructure based on the use of three-dimensional X-ray microtomography images, these tests

* Corresponding author.
E-mail address: pierre.dumont@insa-lyon.fr (P.J.J. Dumont).

enabled the effects of fibers on the rheology and on the microstructure of the resulting fresh mortar to be estimated at a fixed strain rate. These tests also enabled a better understanding of the interactions between the rheology, the microstructure, and the physical properties of the hardened render. The main conclusions that have been reported by Chalencon et al. (2010) [17] are as follows:

(1) The initial porous microstructure and granulometry of the render did not depend on the fiber content, nor the fiber orientation.
(2) For moderate strain rates, i.e., $D_{33} = 10^{-1}$ s^{-1}, compression had a weak influence on the evolution of the microstructure. The porous and fibrous phases did not evolve: the 2D planar random orientation of the fiber was maintained and the macro-pore size distribution ranged from 50 and 600 μm in diameter and was centered on 200 μm, before and after compression.
(3) The stress levels increased with the fiber volume fraction f and the fiber aspect ratio r. However, the influence of the fiber reinforcement on the axial compression stress did not depend on the axial compression strain. For the HP fiber bundles (aspect ratios that ranged from 40 to 455), this evolution could be modelled by adopting a theoretical framework developed for incompressible semi-dilute Newtonian suspension of well dispersed and straight fibers [19,20]. On the contrary, this approach did not work for the HD fiber bundles (aspect ratios of 400 and 793). The potential origin of this behavior could be (i) the limited bending stiffness of the fibers (the HD fiber bundles disaggregated which resulted in nearly completely individualized glass filaments that could easily bend during flow [17], and thus limit the increase in the stress level compared to perfectly straight fibers) and (ii) the clusters of fibers that remained after processing.

In this previous study only one strain rate was tested. However, renders are subjected to high strain rates during the spraying stage: $D_{33} \approx 10$ s^{-1}. In some "dead zones" of the processing or spraying apparatuses, the strain rate can be very small values. The strain rate can also be very small if the renders slide on their substrate ($D_{33} \approx 10^{-5}$ s^{-1}). Hence, in this study, new rheometry experiments were performed using the same render in a wider range of applied strain rates for several fiber fractions to better investigate the coupling between these parameters and the flow-induced microstructures. For that purpose, the porous and fibrous microstructure of renders was studied using X-ray microtomography. X-ray micrographies were also used to estimate the permeability of renders by direct pore scale flow numerical simulations, which allowed us to illustrate the important coupling between the flow-induced microstructure of renders and one of their main end-use properties. These experiments also enabled a workability domain to be defined for renders based on the microstructure of their fibrous reinforcement and the imposed flow conditions.

2. Compression rheometry

2.1. Materials

The self-reinforced render was made up of a dry pre-mix composed of more or less spherical grains of various sizes and natures (polymers, cement, silica fillers, and sand limestone) and glass fiber bundles [17]. After pouring water in the granular pre-mix, the polymer was dispersed, air bubbles formed, and the as-obtained mixture formed a porous and concentrated granular suspension with a porosity of 17% in the fresh state [17]. For all rheological experiments, time t_0 was the initial time of the sample after 3-min mixing of the mortar constituents and 10-min rest.

The two types of fiber bundles were different because of their sizing, which enabled the HP fiber bundles not to disintegrate during both the processing and the rheological experiments, and the HD fiber bundles to disintegrate and to disperse in the render. The cross section of fiber

bundles was initially composed of more than 200 fibers with a 14 μm diameter. The cross section dimensions were precisely measured by following a procedure reported by Chalencon et al. [17]. The cross section of the bundle could be represented by an ellipse with a minor axis $d_{min} \approx 50$ μm and a major axis $d_{max} \approx 400$–800 μm. Four bundle lengths l were used in this study for the HP fiber bundles: 6.1, 10.9, 20.9, and 72 mm, and three lengths for the HD fiber bundles: 5.6, 11.1, and 24 mm. Consequently, the aspect ratio $r = l/\sqrt{d_{min} d_{max}}$ of bundles ranged between 40 and 1700. Four mass fractions of fiber bundles were also used, i.e., $f_w = 0.005, 0.01, 0.02,$ and 0.04, corresponding to fiber volume fractions $f = 0.003, 0.007, 0.014$ and 0.027, respectively. Note that the fiber volume fraction was estimated from the fiber mass fraction and the specific masses of the fibers and the mortar without fiber.

The specific processing route reported by Chalencon et al. [17] was used to prepare cylindrical samples of self-reinforced render with controlled initial microstructure (planar random fiber orientation distribution and initial porosity of 17%) and restrained variability. As reported in Chalencon et al. [17], the global density and the local porosity of the samples did not exhibit any significant variations with the fiber content and the fiber type.
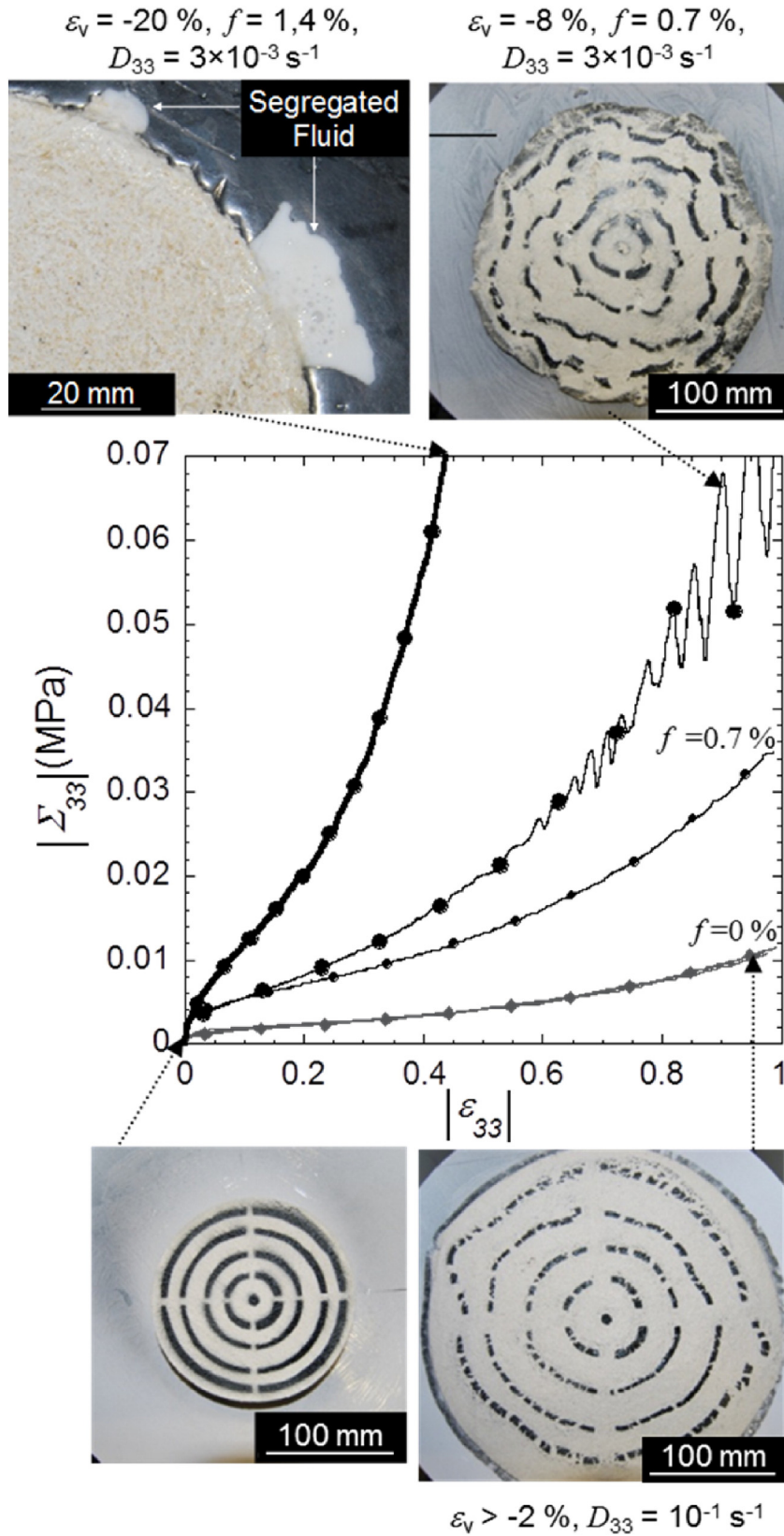
2.2. Compression tests

The rheology of the self-reinforced render was studied using a simple compression rheometer that was initially developed for studying the rheology of highly concentrated fiber suspensions such as fiber-reinforced polymers [21–24,46] and that was adapted for fiber-reinforced mortars [17]. Experiments consisted of compressing lubricated cylindrical samples (initial diameter D_0, initial height h_0) at constant axial average strain rate, $D_{33} = \dot{h}/h$, between two parallel horizontal plates. Four strain rates D_{33} were set at $1, 0.1, 0.01,$ and 0.003 s^{-1} on the basis of the cross-head velocity capacity of the testing machine. Note that these strain rates were in the range of potential strain rates the render could be subjected to during processing. The height h and the axial load F_3 were recorded during compression and were used to calculate the average axial logarithmic compression strain $\varepsilon_{33} = \ln(h/h_0)$ and the nominal compression stress $\sum_{33} = 4F_3/(\pi D_0^2 h_0)$. The final height h_f and the final diameter D_f of deformed cylindrical samples were also measured so that the volumetric strain $\varepsilon_v = \ln(h_f D_f/(h_0 D_0))$ of each sample after compression was estimated.

3. Rheometry results

3.1. Flow regimes

Fig. 1 shows four typical compression stress–strain curves obtained for the reference render (without fiber) and two self-reinforced renders ($f = 0.7$ and 1.4%) at two strain rates ($D_{33} = 0.1$ and 0.003 s^{-1}).

- The gray curve was obtained for a non-reinforced render at a moderate strain rate $D_{33} = 0.1$ s^{-1}. The measured volumetric strain ε_v was higher than -2%, showing that the compression deformation was nearly isovolume. For the same strain rate, adding HD fibers ($f = 0.7\%$, $r = 793$) induced an increase of the compression stress, but again the volumetric strain remained lower than 2%. The photographs show the concentric circles drawn on the upper surface of the specimens also remained circular and concentric during compression, and followed homothetic transformation. These observations demonstrated that, thanks to lubrication, the flow was homogeneous at the macroscopic scale.
- For $f = 0.7\%$ and a lower strain rate, i.e., $D_{33} = 0.003$ s^{-1}, the stress level increased sharply. This phenomenon was accompanied by a large volume strain $\varepsilon_v = -8\%$, showing that the sample was consolidated during the compression experiment. The circular marks drawn on the upper surface of the deformed sample also revealed

Fig. 1. Typical lubricated compression tests performed at various strain rates using the render without fibers or with HD fibers ($r = 793$). Stress–strain curves $\Sigma_{33} - \varepsilon_{33}$ were obtained from four tests performed using three fiber volume fractions ($f = 0\%, 0.7\%, 1.4\%$) and two strain rates ($D_{33} = 10^{-1}, 3 \times 10^{-3}\ s^{-1}$). Pictures show top views of the initial shape and deformed shapes ($\varepsilon_{33} = 1$) of samples in various testing conditions.

local rotations that were induced by the fibers [22,23]. However, these circles remained more or less concentric, showing that the flow was still elongational at the macroscopic scale.

• For $f = 1.4\%$ and HD fibers ($r = 793$) and a slow strain rate ($D_{33} = 0.003\ s^{-1}$), the axial stress showed a pronounced increase with the axial strain. This phenomenon was accompanied by a large reduction

of the sample volume ($\varepsilon_v < -20\%$) and the segregation of a white liquid that is shown in the image of the deformed sample. This liquid was composed of 70% in weight of water, polymer, and cement as it was revealed by thermogravimetric analysis.

Hence, three flow regimes were identified: isovolume flow, consolidating flow, as well as consolidating and segregation flow. These regimes depend on the reinforcement, *i.e.*, fiber type, fiber aspect ratio and fiber volume fraction, and on the applied strain rate.

3.2. Influence of fiber volume fraction and aspect ratio on flow regimes

The respective influence of the fiber content *f* and the aspect ratio *r* on the rheological behavior was investigated for strain rates $D_{33} = 0.003 \text{ s}^{-1}$ and $D_{33} = 0.1 \text{ s}^{-1}$ (only the influence of *r* for the HD fiber type was shown for the second strain rate). All results are gathered in Fig. 2(a–d). These graphs show the evolution of the dimensionless nominal axial stress $\sum^*$, obtained from the ratio between $\sum_{33}$ recorded for the current render formulation and $\sum_{33}$ recorded for the so-called reference formulation, as a function of the axial strain rate D_{33}:

$$\sum^* = \frac{\sum_{33}(\text{type of reinforcement}, f, r)}{\sum_{33}(\text{mortar without reinforcement})}. \tag{1}$$

Using this figure and the measurement of the volume strain ε_v, the conditions that led to the three aforementioned flow regimes for all formulations and testing conditions were identified:

(1) **Isovolume flow**: this flow regime was characterized by weak volume strain ε_v, typically $\varepsilon_v > -2\%$ at the end of the experiment. This flow regime was also characterized by a nearly constant evolution of the dimensionless nominal stress $\sum^*$. From a phenomenological point of view, this regime was observed
- For a decrease in the volume fraction of fibers *f*. For instance, graphs a and b in Fig. 2 show that this regime was present at a strain rate $D_{33} = 0.003 \text{ s}^{-1}$ for all volume fractions lower or equal to 1.4% for HP fibers ($r = 58$) and 0.3% for HD fibers ($r = 793$), respectively.
- For a decrease in the aspect ratio of fibers *r*. Graph c in Fig. 2 shows that this regime was obtained at $D_{33} = 0.003 \text{ s}^{-1}$ for aspect ratios lower or equal to 144.
- For an increase in the strain rate D_{33}. For instance, for slender HD fibers ($r = 793$), this flow regime was present at moderate strain rates for fiber volume fractions lower or equal to 0.7% (graph d in Fig. 2). This limit in fiber volume fraction decreased to 0.3% for low strain rates (graph b in Fig. 2). For moderately slender HP fibers ($r = 58$), this regime was always present at
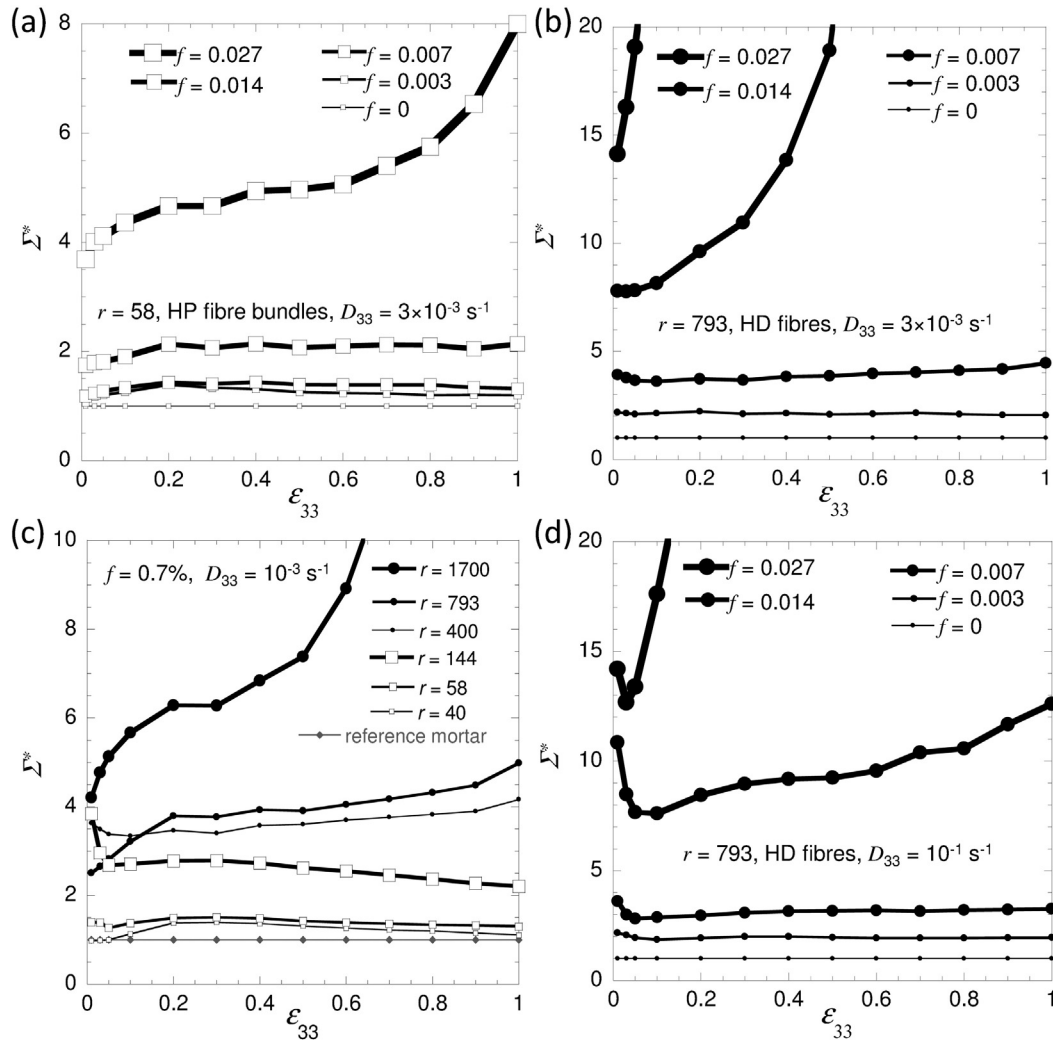
Fig. 2. Evolution of the rheological behavior of the render with the fiber volume fraction *f* (a, b, d) and the aspect ratio *r* (c). Graphs show the evolution of the dimensionless axial stress Σ^* as a function of the axial strain ε_{33} for fiber aspect ratio $r = 58$ and strain rate $D_{33} = 3 \times 10^{-3} \text{ s}^{-1}$ (a), fiber aspect ratio $r = 793$ and strain rate $D_{33} = 3 \times 10^{-3} \text{ s}^{-1}$ (b) or strain rate $D_{33} = 10^{-1} \text{ s}^{-1}$ (d), fiber volume fraction $f = 0.7\%$ and strain rate $D_{33} = 3 \times 10^{-3} \text{ s}^{-1}$ (c). Results for HP fibers bundles are represented by white symbols, whereas HD fibers are represented by black symbols. These rheometry results complete those reported by Chalencon *et al.* [17].

moderate strain rates regardless of the studied fiber volume fractions [17] and disappeared for greater fiber volume fractions and low strain rates (graph a in Fig. 2).

(2) **Consolidating flow**: this flow regime occurred for greater volume fraction of fibers, greater aspect ratio of fibers, and weaker strain rates. The consolidating flow regime was characterized (i) by an important volume decrease, typically reaching $-10\% < \varepsilon_v < -2\%$ at the end of the experiment, and (ii) by a weak to moderate increase of the dimensionless nominal stress $\sum^*$ as a function of the compression strain ε_{33}. For instance, Fig. 2 shows that this flow regime was reached for suspensions made up of weakly slender HP fibers with a great volume fraction of fibers $f = 2.7\%$ that were compressed at low strain rates (graph a), of HD fibers ($r = 793$) with a volume fraction of fibers $f = 0.3\%$ or 0.7% (graphs b and d, respectively) that were compressed at weak or moderate strain rates. Regardless of the type of fibers, this regime was also reached for all suspensions containing a moderate volume fraction of fibers ($f = 0.7\%$) with a large aspect ratio ($r = 400$, graph c).

(3) **Consolidating and segregating flow**: further decreasing the strain rate and/or increasing the volume fraction of fibers and/or increasing the aspect ratio of fibers, a new flow regime occurred. In this new regime, (i) the consolidation was strong, i.e., $-20\% < \varepsilon_v < -10\%$, (ii) the increase of the dimensionless stress $\sum^*$ was extremely large: see, for instance, the results that were obtained for the strongest volume fraction of fibers shown in graphs a, b, and d and the strongest fiber aspect ratio in graph c. Note that these phenomena have already been reported during extrusion of other types of cement-based pastes [58]

3.3. Isovolume flow regime: influence of the compression strain rate

Two other strain rates $D_{33} = 1$ s^{-1} and $D_{33} = 0.01$ s^{-1} were used in this section to complete the previous results that were obtained for a fiber volume fraction $f = 0.7\%$ of weakly slender HP fiber bundles ($r = 58$):

- First, regardless of the reached strain, the volume strains ε_v of each deformed sample were weak and larger or equal to –2%. So, for all testing conditions, the flow was isovolume.
- Fig. 3 shows that the dimensionless nominal stress $\sum^*$ was also independent of the compression strain ε_{33}.
- Fig. 3 also shows that the dimensionless nominal stress $\sum^*$ did not depend on the strain rate D_{33}. Thus, the effect of the fibrous reinforcement on the rheological behavior of render was to homogeneously increase the stress level, independently of the compression strain ε_{33} and the strain rate D_{33}.

According to these results, the compression stress $\sum^f_{33}$ can be written as a function of the compression strain in isovolume flow conditions as follows:

$$\sum^f_{33} = \sum^{(0)}_{33}(D_{33}, \varepsilon_{33})\sum^*_0 \sum^*. \tag{2}$$

This expression has already been proposed by Chalencon et al. [17]. The compression stress $\sum^f_{33}$ mainly depends on the stress $\sum^{(0)}_{33}$ seen by the non-reinforced render, which depends on the compression strain ε_{33}, and the strain rate D_{33}. The compression stress $\sum^f_{33}$ is also modified by (i) an ageing stress $\sum^*_0$ [10–12,17], which is here independent of the render formulation (reinforced render or not) [17], and by (ii) a fibrous reinforcement stress $\sum^*$, which depends on the type, the volume fraction and aspect ratio of fibers. As reported by Chalencon et al. [17], the stress $\sum^*$ can be modeled using expressions for semi-dilute Newtonian fiber suspensions.
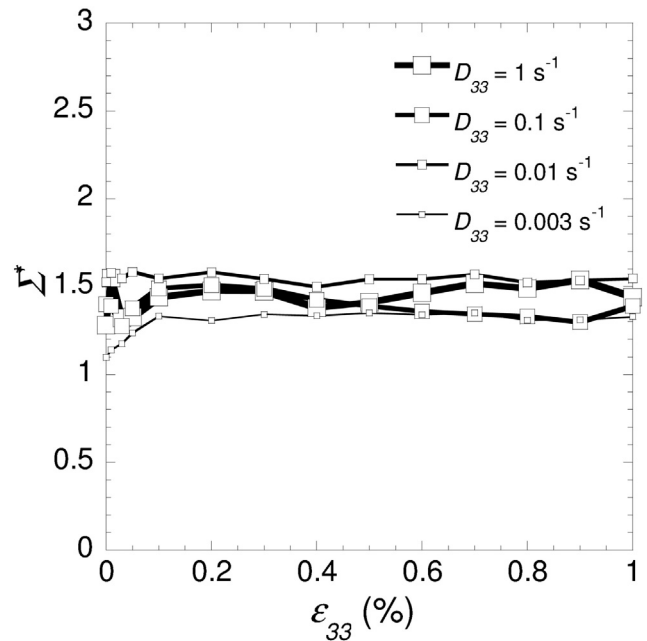
Fig. 3. Dimensionless axial stress Σ^* as a function of the strain rate for the isovolume flow regime ($f = 0.7\%$, $r = 58$, HP fibers).

4. Initial and flow-induced microstructures for the various regimes

4.1. Local densities profiles

Local density profiles were assessed along the radius of several typical samples 48 h after t_0, i.e., after they were solidified, by measuring their weight in air and then while submerged in water. The first sample contained HD fibers ($r = 793$, $f = 0.007$) and was deformed at $D_{33} = 0.1$ s^{-1} in the first flow regime. The second sample also contained HD fibers but was deformed in the second flow regime at $D_{33} = 0.003$ s^{-1}. The third sample also contained HD fibers ($r = 793$, $f = 0.014$) and was deformed in the third regime at $D_{33} = 0.003$ s^{-1}. Fig. 4 shows the corresponding density profiles.

- For the isovolume flow regime (regime 1), the density of 1.45 ± 0.02 was spatially homogeneous and equal to that of the non-deformed sample.
- For the consolidating flow regime (regime 2), the sample became denser. The average density reached up to 1.56. The density also decreased from the center to the outer radius of the sample.
- For the consolidating and segregating flow regime (regime 3), the average density further increased and reached a maximum of 1.82. The density gradient was also more pronounced than in the consolidating flow regime. Note that the density that was reached on the outer radius of the sample was even lower than the density of the first sample corresponding to the first flow regime. The migration of the liquid phase that was rich in water from the center of the sample to its edge and the subsequent evaporation of this phase during solidification was probably at the origin of the local increase of the sample porosity.

4.2. X-ray microtomography analysis

Figs. 5 to 7 show 3D micrographies that were obtained at $t_0 + 24$ h by 3D X-ray microtomography and the results of images analysis performed using small cubic volumes that were also used for the measurements of local density for each flow regime. These small cubes were
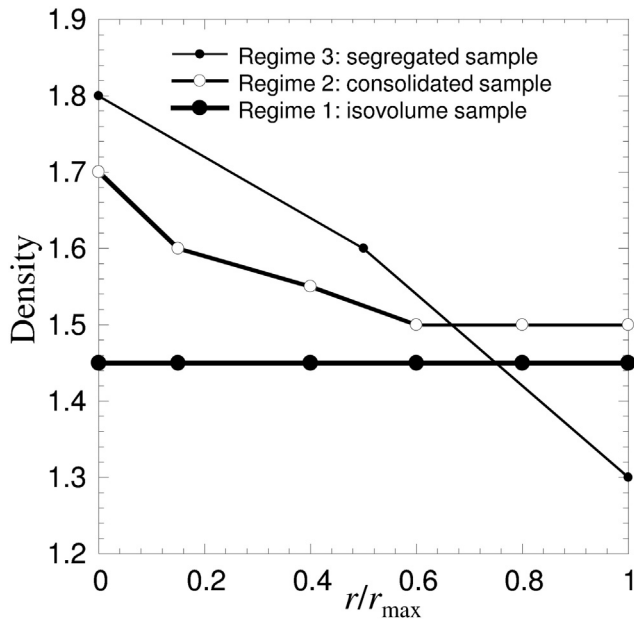
Fig. 4. Density profiles along the normalized radius r/r_{max} (where r_{max} is the external radius of the studied samples) measured from the center to the edge for three samples corresponding to the three flow regimes.

extracted at the center and at the side of the compressed samples. A laboratory microtomograph (Phoenix Vtomex, INSA-Lyon) was used to acquire these images. A total of 720 X-ray 2D projections of the samples was acquired during the scans. These projections were obtained by incrementally rotating the samples in front of the X-ray source (scanning time of approximately 30 min, 90 kV, 140 mA). Then three-dimensional maps of the X-ray absorption coefficient were reconstructed for each sample (volumes of maximal size of $2000 \times 2000 \times 1500$ voxels, voxel size = 6 μm). Images that correspond to regimes 1, 2, and 3 are given in Figs. 5, 6, and 7, respectively. All details of the measurement protocol are reported by Chalencon et al. (2010) [17]. In each figure, the volumes in gray levels of the center (a) and of the edge (b), the corresponding segmented porous phase of the center (c) and of the edge (d), and the corresponding segmented fibrous phase of the center (e) and of the edge (f), are shown:

- The qualitative comparison of the three-dimensional images obtained in gray levels for the various flow regimes confirmed the microstructural homogeneity of the renders between the center and the edge of the sample for regime 1 (Fig. 5a, b). This comparison also confirmed the moderate and severe consolidations that were revealed by rheometry tests or the measurements of local density for regimes 2 and 3, respectively, as the sample porosity greatly decreased at the center of the sample (Figs. 5–7(a)), whereas the porosity moderately changed at the edge of the sample (Figs. 5–7(b)).
- Despite the moderate quality of the 3D images and the large number of various phases, which hindered the segmentation of the fibrous phase, and regardless of the flow regimes, fibers clearly appeared as being planar orientated in Figs. 5–7(e, f). Note also the presence of several clusters of HD fibers. The origin of these clusters was certainly a bad scattering of HD fiber bundles during mixing. The fibrous microstructure also appeared denser and more disaggregated at the center than at the edge of the sample for regime 3 (Fig. 7(e, f)). However, this observation should be confirmed using images with an enhanced quality.
- The porosity of the imaged samples was quantitatively obtained using the segmented images of the porous phase (Figs. 5–7(c, d)). The volume fraction of pores that were larger than 6 μm drastically decreased

during deformation at the center of samples for regimes 2 and 3, whereas this porosity did not evolve for regime 1 and was approximately 30%, 15%, and 7% for regimes 1, 2, and 3, respectively. At the sample edge, the porosity did not change as much, as it was 30%, 29%, and 31% for regimes 1, 2, and 3, respectively.
- Still using the segmented images of the porous phase (Figs. 5–7(c, d)), the pore size distribution was also estimated for pores larger than 48 μm and for all flow regimes [17,18]. Fig. 8(a) shows that the isovolume flow regime (regime 1) did not practically have any effect on the pore size distribution. This observation has already been reported by Chalencon et al. (2010) [17] for this type of flow regime. The same remark holds for the edge of deformed samples for regimes 2 and 3 (Fig. 8(b,c)). In contrast, the pore size distribution greatly changed at the center of deformed samples for regimes 2 and 3 during deformation, as shown in Fig. 8(b, c). This phenomenon was more pronounced for regime 3. For instance, the pore size distribution that was obtained for the consolidating and segregating flow regime 3 was sharper and centered over a smaller pore size ($d_{pores} = 100$ μm) than for the moderately consolidating flow regime 2 ($d_{pores} = 150$ μm).

5. Flow regimes and render workability

Three flow regimes were identified for the fiber self-reinforced renders. These regimes depend on the fiber fraction and aspect ratio as well as on the compression strain rate these granular and porous fiber suspensions are subjected to. It must be pointed out that these flow regimes are likely to occur in practical processing conditions since we have observed them for fiber contents and aspect ratios as well as for strain rates typically encountered in practice.

The first flow regime is isovolume, homogeneous, and one phase. This behavior is mainly inherited from the complex rheological behavior of render without fibers. The microstructural properties of the render associated with this flow regime are homogeneous and remain close to that of the microstructure of the non-deformed render. This flow regime is preferential for all the use operations of render, from its manufacturing to its placement.

The two other flow regimes correspond to deformation modes that are heterogeneous, compressible, and multiphase. Stress levels needed to make the render flow are higher than those required for the first flow regime. Thus, the last two flow regimes should be avoided during processing and placement. This conclusion is reinforced by the drastic changes in the microstructure and in the resulting end-use physical properties of render, for instance, permeability (see next section). Note that these types of deformation modes have been qualitatively reported for granular saturated suspensions [25–35], concentrated fiber suspensions [36–41] and fresh reinforced cement materials [4,8,9,14,56–58]. However, micro-mechanisms at the origin of these flow regimes are not well known. To date, only macroscopic, phenomenological, and multiphase modeling approaches based on mixture theories [42,43] are proposed for the prediction of these phenomena.

For the studied renders and the investigated strain and strain rate regimes, one of the potential microstructural origins of the aforementioned flow phenomena could be attributed to the entanglement of fibers, which may restrain the mortar flow. This mechanism is well known for concentrated fiber suspensions [24]. A similar mechanism is involved in cement-based materials [9,10]. The entanglement of fibers in the render structure is closely related to the number of fiber–fiber contacts per fiber C_f, here estimated using the tube model [44,45,47] as follows:

$$C_f = 4f\left(\frac{2}{\pi}r\Phi_1 + \Phi_2 + 1\right). \tag{3}$$

Isovolume sample: $\varepsilon_v > -2$ %, HD fibres, $f = 0.7\%$, $D_{33} = 10^{-1}$ s^{-1}

Centre   Edge
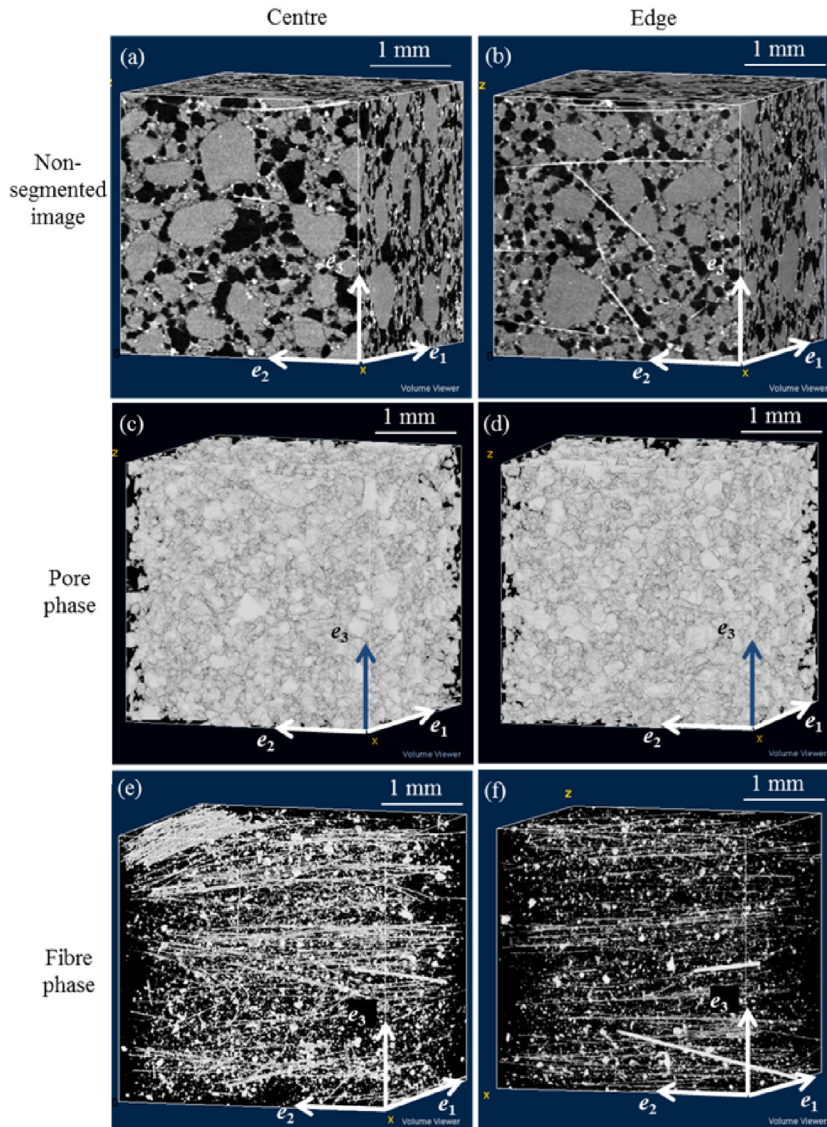
Fig. 5. Three-dimensional micrographs obtained using X-ray microtomography showing the microstructure of the isovolume sample (HD fibers, $f = 0.7\%$, compression strain rate $D_{33} = 10^{-1}$ s^{-1}). Panels a and b show the non-segmented images of the render microstructure. Panels c and d show the segmented porous phase of the same sample, whereas panels e and f show its segmented fibrous phase. Images on the left-hand side show the sample center and images on the right-hand side show the sample edge.

This compact expression of the fiber connectivity shows that C_f is an affine function of the content f, aspect ratio r, as well as the orientation of fibers, *i.e.*, the orientation functions Φ_i ($\Phi_i = 2/\pi$ for planar fiber orientation).

Fig. 9(a) shows the evolution of C_f as a function of f for all aspect ratios r of all types of fibers used in this study (white symbols are used for HP fibers, whereas black symbols are used for HD fibers, the size of the symbols being proportional to the fiber aspect ratio). For $C_f < 1$, the suspensions can be considered to be semi-dilute, *i.e.*, some rare fibers are in contact. For $C_f > 2$ (gray area in the graph in Fig. 9(a)), the suspensions are concentrated as the fibers form a fully interconnected network. Thus, the motion of each fiber becomes increasingly hindered by the presence of the neighboring fibers as C_f increases.

Fig. 9(b) is a "workability" diagram that is useful for practical applications. Indeed, this figure shows the domains that were experimentally identified for the three aforementioned flow regimes in a diagram where the compression strain rate D_{33} is represented versus the number

of contacts C_f for all types of fibers. This diagram shows that a too important increase in C_f leads to the consolidating flow regime 2 that first arose at the lowest compression strain rates for $C_f \approx 2$. Then an increase in C_f eventually leads to the segregating flow regime 3. This flow regime was always observed for $C_f > 15$ over the range of tested compression strain rates D_{33}. Note also that HD fibers preferentially led to flow regimes 2 and 3, whereas the less slender HP fibers mostly led to regime 1. In addition, the higher the strain rate, the larger was the workability zone, *i.e.*, regime 1.

6. Permeabilities of flow-induced render microstructures

As pointed out in Section 4, the formulation of the renders as well as flow conditions have drastic effects on the render microstructure and consequently on their use properties, for instance, their permeability. To illustrate these effects, we estimated the permeabilities of the renders in their hardened state, using (i) the 3D images shown in Figs. 5–7(a, b), (ii) the theoretical framework of the homogenization

Consolidated sample: ε_V = -8 %, HD fibres, f = 0.7%, D_{33} = 3×10^{-3} s^{-1}
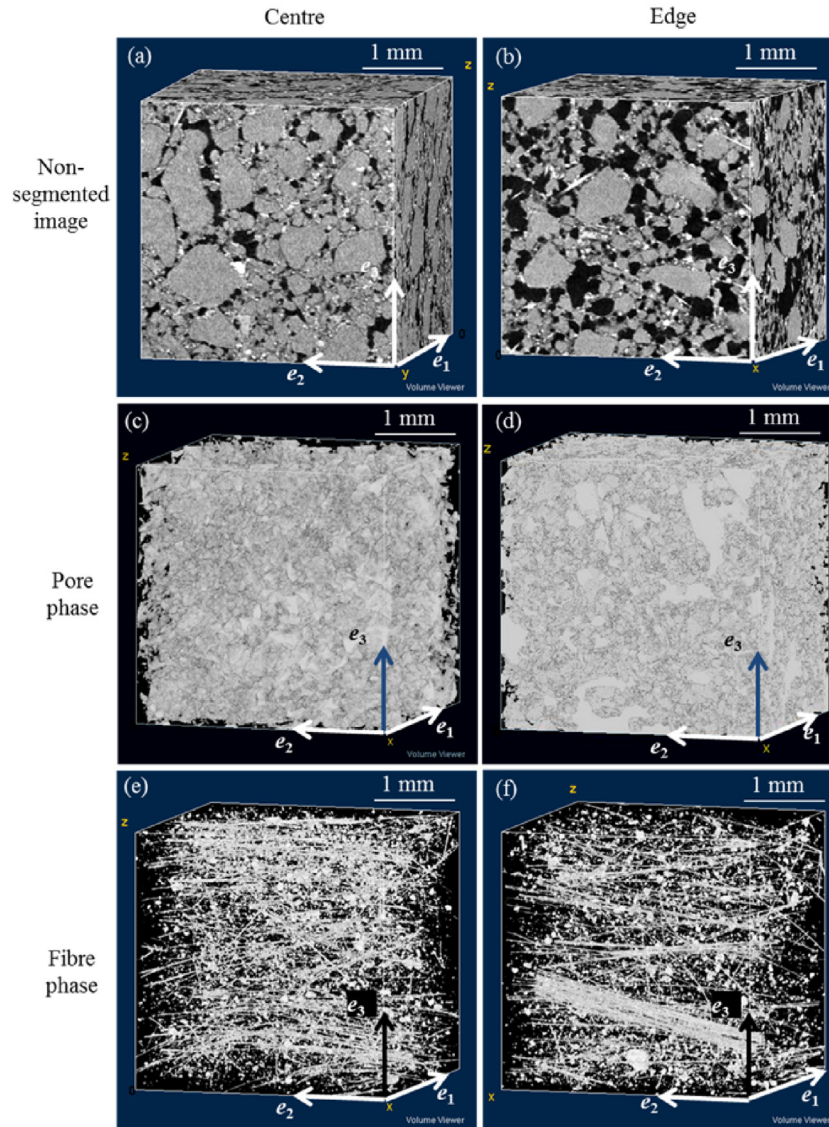
Fig. 6. Three-dimensional micrographs obtained using X-ray microtomography showing the microstructure of a consolidated sample (HD fibers, f = 0.7%, compression strain rate D_{33} = 3×10^{-3} s^{-1}). Panels a and b show the non-segmented images of the render microstructure. Panels c and d show the segmented porous phase of the same sample, whereas panels e and f show its segmented fibrous phase. Images on the left-hand side show the sample center and images on the right-hand side show the sample edge.

method with multiple asymptotic expansions [48–50], (iii) and pore scale fluid flow numerical simulation using the 3D images. This approach has already been successfully used to estimate the permeability of porous materials such as papers [51–53], fibrous reinforcements of composite materials [59], or snow [60]. Details related to this procedure are provided in Appendix 1. In practice, the pore scale fluid flow simulations were performed using the software GeoDict, well adapted for solving Stokes localization problems using segmented 3D images as calculation volumes. The problem was numerically solved using a finite volume method where each voxel of the images represented a finite volume. Volumes of $600\times600\times600$ voxels of the studied render for each flow regime were used to perform the permeability calculations. These volumes were subdivided in eight cubic sub-volumes i of $300\times300\times300$ voxels to reduce the number of degrees of freedom to a maximum of 10^8. The components of the permeability tensor were calculated for each sub-volume. As the principal components of the permeability tensor were close to each other for all sub-volumes, an average permeability k_i was defined for each sub-volume and the permeability k of the entire volume was calculated as the average of

all permeabilities k_i. The as-calculated permeabilities k corresponded to a statistic determination of the permeability of the studied render [55]. Finally, adimensional permeabilities were also calculated as follows:

$$k_i^* = k_i/k_{\text{init}} \text{ and } k^* = k/k_{\text{init}}, \tag{4}$$

where $k_{\text{init}} = 6.8\times10^{-12}$ m^{-2} was the average permeability of the non-deformed render. The dimensionless permeabilities k_i^* (small marks) and k^* (big marks) are plotted in Fig. 10 as a function of the porosities Φ_i or Φ of their corresponding volumes. Each type of marks represents samples that were deformed in one of the three identified flow regimes. The black marks represent volumes that were extracted at the center of the samples of render, whereas the white marks represent samples that were extracted at the edge of the samples.

- For all scanned volumes, the heterogeneity of the render microstructure is illustrated by the large scattering of the porosities Φ_i that were obtained for the sub-volumes compared to the porosity Φ for

Segregated sample: $\varepsilon_V = -20\%$, HD fibres, $f = 1.4\%$, $D_{33} = 3 \times 10^{-3}$ s^{-1}

Centre   Edge
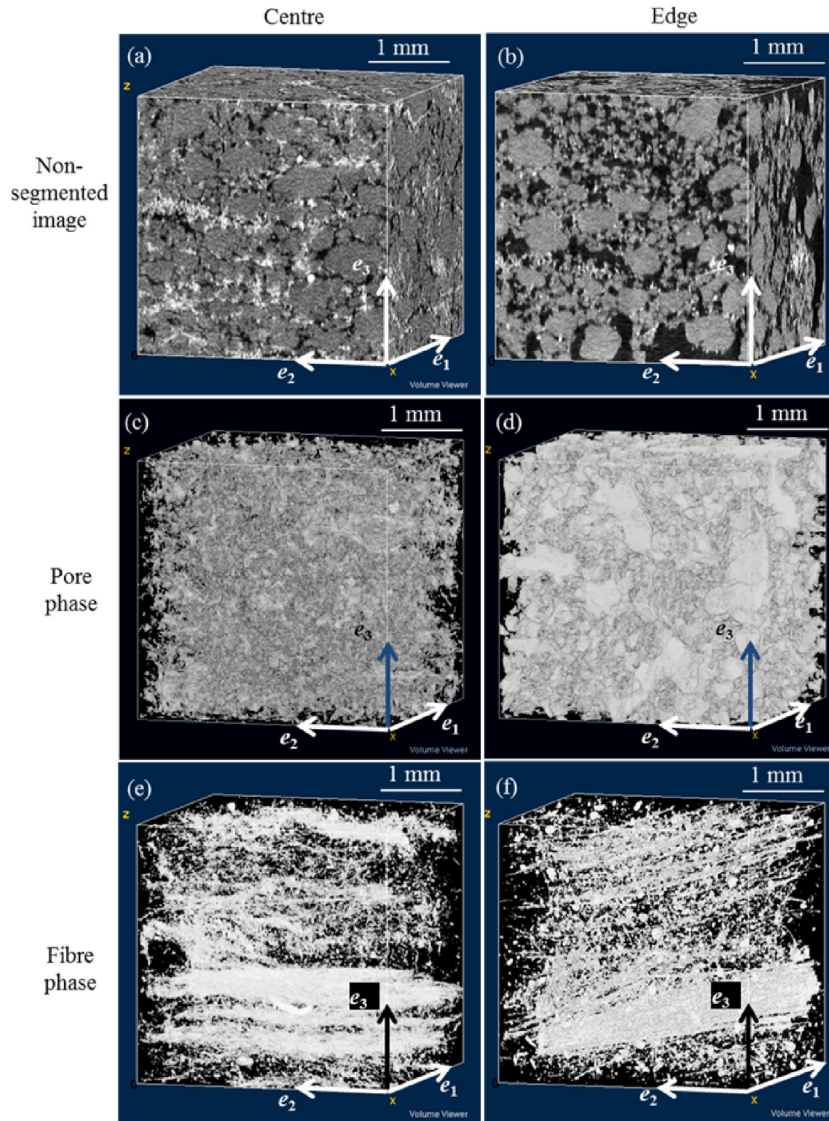
Fig. 7. Three-dimensional micrographs obtained using X-ray microtomography showing the microstructure of a segregated sample (HD fibers, $f = 1.4\%$, compression strain rate $D_{33} = 3 \times 10^{-3}$ s^{-1}). Panels a and b show the non-segmented images of the render microstructure. Panels c and d show the segmented porous phase of the same sample, whereas panels e and f show its segmented fibrous phase. Images on the left-hand side show the sample center and images on the right-hand side show the sample edge.

the entire volumes. This microstructural heterogeneity resulted in a large scattering of the permeabilities k_i^* compared to the permeability k^*.

- The permeabilities k^* of volumes that were extracted from the samples that were deformed in the isovolume flow regime (regime 1) and from the edges of samples that were deformed in the consolidating flow regime (regime 2) or in the segregating flow regime (regime 3) were very close to each other. These permeabilities were also very close to the permeabilities for the non-deformed samples. The porosity and the pore size distribution for all these samples were in a narrow range for all these samples, which explained this result.

- For flow regimes 2 and 3, volumes that were extracted from the center of samples exhibited large microstructural rearrangements. These changes resulted in a sharp decrease in the permeabilities of the render. In regime 2, the permeability was divided by 10 compared to the permeability of the non-deformed render, whereas the permeability was divided by 100 in regime 3.

The render permeabilities were also compared to the static k_s^* and kinematic k_k^* estimates for granular systems proposed by Boutin [50] (see Appendix 2 for their expressions). Fig. 10 shows that these estimates are very close in the considered porosity domain. Note also that all the numerical values that were estimated using the sub-volumes and the entire volumes were also close to the analytical predictions. This shows that these estimates could be used as good first-order analytical predictors of the render permeability.
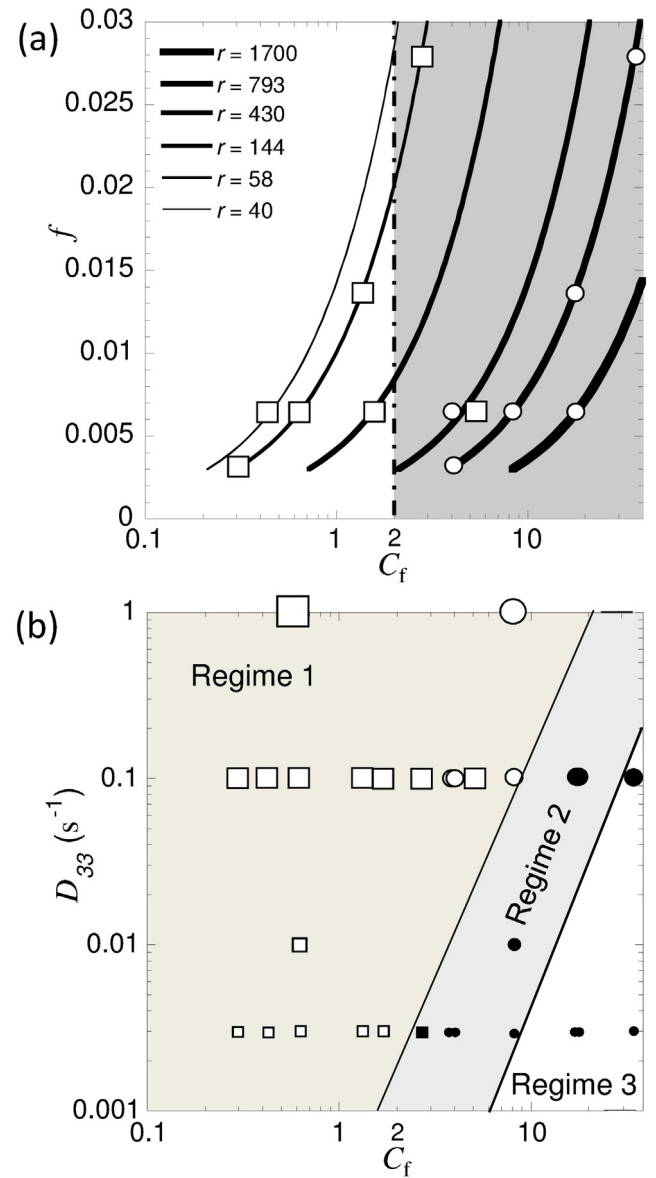
7. Conclusion

In this study, we investigated by lubricated compression tests the rheology of a fiber-reinforced cement mortar used as render for external wall insulation. The analysis was achieved using strain rates, fiber contents, and aspect ratios representative to those experienced in practical conditions. An original use of X-ray microtomography three-dimensional images enabled the microstructural modifications to be finely measured by comparing the porosity and the pore size
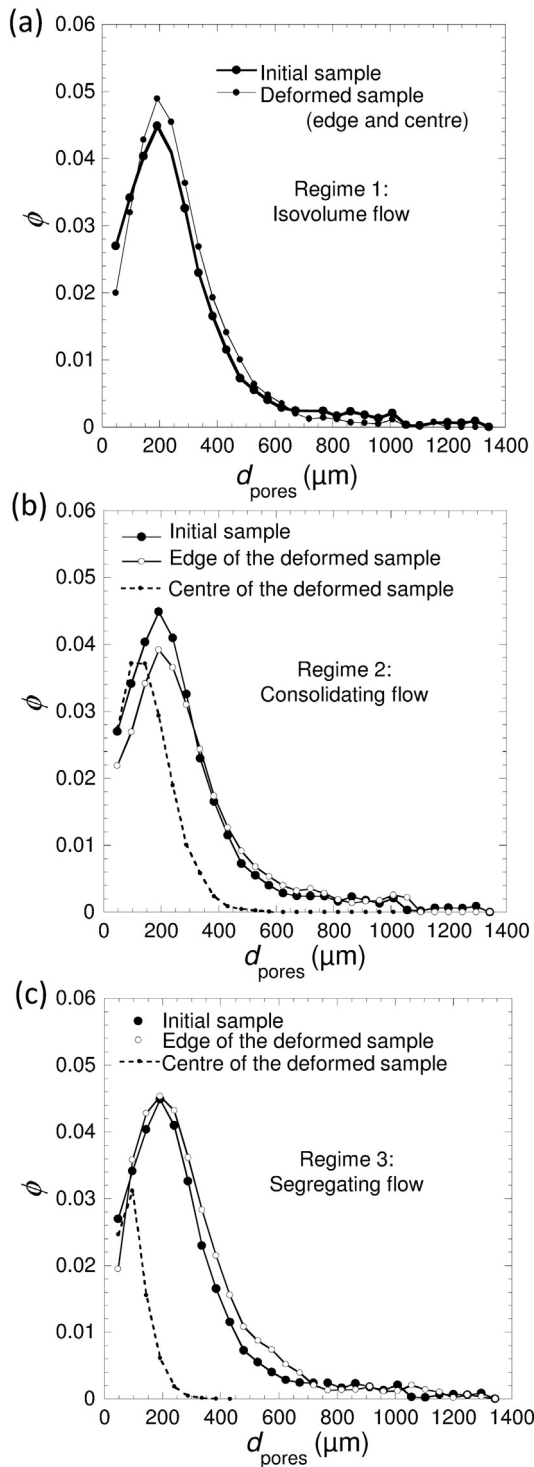
Fig. 8. Comparison of the pore size distribution ϕ between a non-deformed sample and the center and the edge of three samples that were deformed in the isovolume flow regime 1 (a), the consolidating flow regime 2 (b), and the consolidating and segregating flow regime 3 (c).

Fig. 9. (a) Tube model prediction for the evolution of the fiber volume fraction f as a function of the number of fiber–fiber contacts per fiber C_f and for various fiber aspect ratios r. Square symbols correspond to HP fiber bundles and circular symbols to HD fibers. (b) Regions covered by each of the three observed flow regimes in a $D_{33} - C_f$ diagram. Symbols show all experimental results that were obtained for all types of fibers and all tested strain rates D_{33}. The size of the symbol increases with the strain rate D_{33}. In graph b, white symbols correspond to regime 1, and black symbols to regimes 2 and 3.

distribution in both the non-deformed and the compressed states. These images were also used for numerically and analytically estimating the flow-induced evolution of the permeability of fiber-reinforced renders.

Three flow regimes were revealed: a homogeneous isovolume flow regime and two heterogeneous flow regimes, *i.e.*, a consolidating regime and a consolidating and segregating regime. Typically,

the lower the compression strain rate or the higher the fiber content or the fiber aspect ratio, the higher was the flow heterogeneous, *i.e.*, the higher were the variations of density or those of the porosity and the pore size distribution along the radius of samples. For the consolidating and segregating regime, a liquid phase was also expelled from the granular and porous structure of render. In contrast, the microstructure of the isovolume samples was similar to that of non-deformed samples.

For the isovolume flow regime, the compression stress was split into three contributions. The first contribution was inherited from the behavior of the non-reinforced render, the second one from an ageing effect and the third one from a reinforcement effect due to fibers. The fiber contribution was shown to be strain-rate independent for the isovolume flow regime. In contrast, the compression strain rate affected
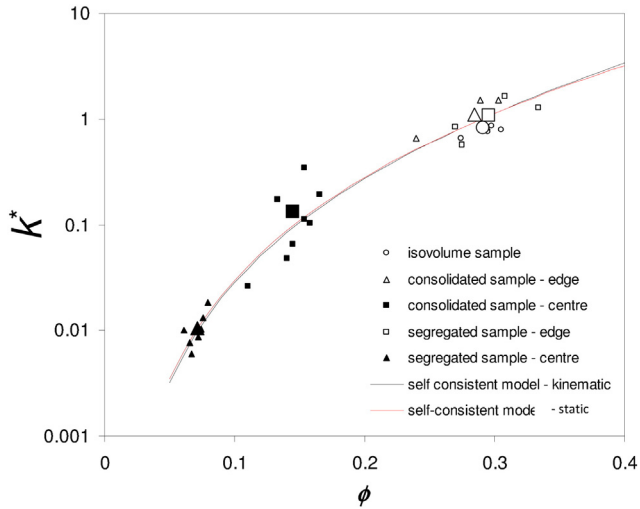
Fig. 10. Evolution of the dimensionless permeabilities k^* that were numerically (symbols) or analytically (continuous lines) calculated as a function of the porosity of the deformed sample for each of the three flow regimes.

the contribution of fibers to the compression stress for the two heterogeneous flow regimes.

We have shown that flow-induced structural modifications drastically affected the render permeability, and thus the performance of EWI systems. Numerical and analytical estimates of the permeability were in accordance. Both approaches showed a decrease in the permeability of the render of two orders of magnitude for the densest samples of the consolidating and segregating flow regime compared to samples of the isovolume flow regime.

The microstructural origin of the flow inhomogeneity was related to the entanglement of fibers within the render granular structure. An increase in the content or in the aspect ratio of fibers corresponding to an increase of the number of fiber–fiber contacts per fiber could lead to the formation of a network of fibers that may hinder the motions of grains.

The observed heterogeneous flow regimes should be avoided. For that purpose, we proposed a workability map showing flow regimes in a diagram of the compression strain rate versus the number of fiber–fiber contacts per fiber, *i.e.*, the two parameters governing the flow regimes. This workability diagram may be useful either for the formulation of the renders or for the prediction of the strain rate range they should be subjected to exhibit isovolume homogeneous flows.

Acknowledgments

Appendix 1

The theoretical framework proposed by the homogenization method with multiple-scale asymptotic expansions gives an equivalent and continuous macroscopic law for the behavior of a complex and heterogeneous porous material, assuming that this medium can be seen as the periodic juxtaposition of a representative elementary volume (REV) Ω and that the size L of the medium exhibits a good scale separation with the size l of the REV, *i.e.*, $\varepsilon = l/L \ll 1$. The prediction of this model for the laminar flow of incompressible Newtonian fluid with viscosity μ in the REV Ω of a connected porous and rigid medium in which the fluid occupies the domain Ω^f and the solid occupies the domain Ω^s

shows that the divergence of the macroscopic equivalent velocity field $\underline{v}^{\text{macro}}$,

$$\underline{v}^{\text{macro}} = \left\langle \underline{v}^{(0)} \right\rangle = \frac{1}{\Omega} \int_{\Omega^f} \underline{v}^{(0)} dV \tag{5}$$

is zero,

$$\text{div}\underline{v}^{\text{macro}} = 0 \tag{6}$$

and that $\underline{v}^{\text{macro}}$ is a function of the macroscopic pressure gradient the medium is subjected to, by the well-known Darcy's law [54] as follows:

$$\underline{v}^{\text{macro}} = -\frac{1}{\mu}\underline{\underline{K}} \cdot \text{grad}p^{\text{macro}}, \tag{7}$$

where $\underline{\underline{K}}$ is the permeability tensor of the equivalent medium. The components of $\underline{\underline{K}}$ are obtained by solving a Stokes-like localization problem on the REV with no-slip boundary conditions at the interface Γ between the fluid domain Ω^f and the solid phase Ω^s [51–53]:

$$\begin{cases} \text{div}\underline{v}^{(0)} = 0 \\ \text{grad}p^{\text{macro}} + \text{grad}\varepsilon p^{(1)} = \mu \Delta \underline{v}^{(0)} \end{cases} \text{in } \Omega \tag{8}$$
$$\underline{v}^{(0)} \cdot \underline{n} = 0 \text{ on } \Gamma \text{ (}\underline{n}\text{ is a normal vector to } \Gamma\text{)}$$

where the pressure gradient $\text{grad}p^{\text{macro}}$ is a constant input. The periodic unknowns $\varepsilon p^{(1)}$ and $\underline{v}^{(0)}$ correspond to the first-order fluctuation of the pressure p and to the order 0 of the velocity field $\underline{v}$, respectively.

The permeability tensor $\underline{\underline{K}}$ is calculated using Eq. (9) by successively imposing:

$$\text{grad}p^{\text{macro}} = \underline{e}_i (i = 1, 2, 3). \tag{9}$$

Appendix 2

Using the homogenization method with multiple scale asymptotic expansions and self-consistent estimates Boutin proposed static k_s^* and kinematics k_k^* estimates for the permeability of granular systems [50]:

$$k_s^* = \frac{\varphi(\Phi)}{\varphi(\Phi_{\text{init}})} \tag{10}$$

and

$$k_k^* = \frac{\Psi(\Phi)}{\Psi(\Phi_{\text{init}})} \tag{11}$$

with

$$\varphi(\Phi) = \frac{1 - \Phi^{1/3}}{18\Phi^{1/3}} \left(4 - 5\frac{\Phi^{1/3}\left(1 + \Phi^{1/3}\right)\left(1 - \Phi^{2/3}\right)}{1 - \Phi^{5/3}} \right) \tag{12}$$

and

$$\Psi(\Phi) = \frac{1 - \Phi^{1/3}}{3\Phi^{1/3}} \left(1 - \frac{1 - \Phi^{5/3}}{\left(1 - \Phi^{1/3}\right)\left(3 + 2\Phi^{5/3}\right)} \right), \tag{13}$$

where Φ_{init} is the porosity of the initial sample.

References

[1] T. Duforestel, P.-H. Milleville, D. de Cacqueray, B. Yrieix, EDF S.A. (2008) (Patent 2.904640, W02008015036, EP2052116, FR290640).
[2] B. Cheng, J. Liu, Contribution of hybrid fibers on the properties of the high-strength lightweight concrete having good workability, Cem. Concr. Res. 35 (2005) 913–917.

[3] P. Banfill, G. Starrs, G. Derruau, W. Mc Carter, T. Chrisp, Rheology of low carbon fiber content reinforced cement mortar, Cem. Concr. Compos. 28 (2006) 773–780.

[4] L. Ferrara, Y.-D. Park, S.P. Shah, A method for mix-design of fiber-reinforced self compacting concrete, Cem. Concr. Res. 37 (2007) 957–971.

[5] L. Ferrara, Y.-D. Park, S.P. Shah, Correlation among fresh state behavior, fiber dispersion, and toughness properties of SFRCs, J. Mater. Civ. Eng. 20 (2008) 493–501.

[6] M. Sahmaran, I.O. Yaman, Hybrid fiber reinforced selfcompacting concrete with a high volume coarse fly ash, Constr. Build. Mater. 21 (2007) 150–156.

[7] K.G. Kuder, N. Ozyurt, E.B. Mu, S.P. Shah, Rheology of fiber-reinforced cementitious materials, Cem. Concr. Res. 37 (2007) 191–199.

[8] Y. Ding, S. Liu, Y. Zhang, A. Thomas, The investigation on the workability of fiber cocktail reinforced self compacted high performance concrete, Constr. Build. Mater. 22 (2008) 1462–1470.

[9] L. Martinie, P. Rossi, N. Roussel, Rheology of fiber reinforced cementitious materials classification and prediction, Cem. Concr. Res. 40 (2010) 226–234.

[10] A. Perrot, T. Lecompte, P. Estellé, S. Amziane, Structural buil-up of rigid fiber reinforced cement-based materials, Mater. Struct. 46 (2013) 1561–1568.

[11] N. Roussel, Steady and transient flow behavior of fresh cement pastes, Cem. Concr. Res. 35 (9) (2005) 1656–1664.

[12] N. Roussel, A thixotropy model for fresh fluid concretes: theory, validation and applications, Cem. Concr. Res. 36 (10) (2006) 1797–1806.

[13] L. Martinie, N. Roussel, Simple tools for fiber orientation prediction in industrial practice, Cem. Concr. Res. 41 (2011) 993–1000.

[14] S. Grünewald, J.C. Walraven, Parameter study on the influence of steel fibers and coarse aggregate content on the fresh properties of self-compacting concrete, Cem. Concr. Res. 31 (2001) 1793–1798.

[15] Y. Akkaya, A. Peled, P. Shah, Parameters related to fiber length and processing in cementitious composites, Mater. Struct. 33 (2000) 515–524.

[16] B. Shen, M. Hubler, G.H. Pauloni, L.J. Struble, Functionally-graded fiber-reinforced cement composite: processing, microstructure and properties, Cem. Concr. Compos. 30 (2008) 663–673.

[17] F. Chalencon, L. Orgéas, P.J.J. Dumont, G. Foray, J.-Y. Cavaillé, E. Maire, S. Rolland du Roscoat, Lubricated compression and X-ray microtomography to analyse the rheology of fiber reinforced mortar, Rheol. Acta 49 (2010) 221–235.

[18] E. Maire, P. Colombo, J. Adrien, L. Babout, L. Biasetto, Characterization of he morphology of cellular ceramics by 3D image processing of X-ray tomography, J. Eur. Ceram. Soc. 27 (2007) 1973–1981.

[19] E.S.G. Shaqfeh, G. Fredrickson, The hydrodynamic stress in a suspension of rods, Phys. Fluids 2 (1) (1990) 7–24.

[20] G.G. Lipscomb, M.M. Denn, D.U. Hur, D.V. Boger, The flow of fiber suspensions in complex geometries, J. Non-Newtonian Fluid Mech. 26 (1988) 297–325.

[21] S. Le Corre, L. Orgéas, D. Favier, A. Tourabi, A. Maazouz, C. Venet, Shear and compression behavior of sheet molding compounds, Compos. Sci. Technol. 62 (2002) 571–577.

[22] P. Dumont, L. Orgéas, S. Le Corre, D. Favier, Anisotropic viscous behavior of sheet molding compounds (SMC) during compression molding, Int. J. Plast. 19 (2003) 625–646.

[23] P. Dumont, J.-P. Vassal, L. Orgéas, V. Michaud, D. Favier, J.-A.E. Månson, Processing, characterization and rheology of transparent concentrated fiber bundle suspensions, Rheol. Acta 46 (2007) 639–651.

[24] L. Orgéas, P.J.J. Dumont, T.-H. Le, D. Favier, Lubricated compression of BMC, a concentrated and fiber reinforced granular polymer suspension, Rheol. Acta 47 (2008) 677–688.

[25] B. Lantéri, H. Burlet, A. Poitou, I. Campion, Powder injection molding: an original simulation paste flow, Eur. J. Mech. A. Solids 22 (7) (1996) 943–968.

[26] N. Delhaye, A. Poitou, M. Chaouche, Squeeze flow of highly concentrated suspensions of spheres, J. Non-Newtonian Fluid Mech. 94 (2000) 67–74.

[27] A. Poitou, G. Racineux, A squeezing experiment showing binder migration in concentrated suspensions, J. Rheol. 45 (3) (2001) 609–625.

[28] J.D. Sherwood, Liquid–solid relative motion during slow squeeze flow of pastes, J. Non-Newtonian Fluid Mech. 128 (2005) 163–171.

[29] F. Chaari, G. Racineux, A. Poitou, M. Chaouche, Rheological behavior of sewage sludge and strain-induced dewatering, Rheol. Acta 42 (2003) 273–279.

[30] N. Roussel, C. Stefani, R. Le Roy, From mini cone test to Abrams cone test: measurement of cement based materials yield stress using slump tests, Cem. Concr. Res. 35 (5) (2003) 817–822.

[31] L. Orgéas, J.-P. Gabathuler, T. Imwinkelried, C. Paradies, M. Rappaz, Modelling of semi solid processing using a modified temperature-dependent power-law model, Model. Simul. Mater. Sci. Eng. 11 (2003) 553–574.

[32] N. Roussel, C. Lanos, Y. Melingeb, Induced heterogeneity in saturated flowing granular media, Powder Technol. 138 (2004) 68–72.

[33] Z. Toutou, N. Roussel, C. Lanos, The squeezing test: a tool to identify firm cement-based material's rheological behavior and evaluate their extrusion ability, Cem. Concr. Res. 35 (2005) 1891–1899.

[34] F.A. Cardoso, V.M. John, R.G. Pileggi, Rheological behavior of mortars under different squeezing rates, Cem. Concr. Res. 39 (2009) 748–753.

[35] F.A. Cardoso, V.M. John, R.G. Pileggi, P.F.G. Banfill, characterization of rendering mortars by squeeze-flow and rotational rheometry, Cem. Concr. Res. 57 (2014) 79–87.

[36] T.A. Osswald, S.C. Tseng, in: S.G. Advani (Ed.), Flow and rheology in polymer composites manufacturing, Elsevier 1994, pp. 361–413 (Chapter 10).

[37] H. Yaguchi, H. Hojo, D.G. Lee, E.G. Kim, Measurement of planar orientation of fibers for reinforced thermoplastics using image processing, Int. Polym. Process. 3 (1995) 262–269.

[38] F. Danès, B. Garnier, T. Dupuis, P. Lerendu, T.-P. Nguyen, Non-uniformity of the filler concentration and of the transverse thermal and electrical conductivities of filled polymer plates, Compos. Sci. Technol. 65 (2005) 945–951.

[39] L. Orgéas, P.J.J. Dumont, V. Michaud, D. Favier, Separation of the polymer matrix and the fibrous reinforcement during compression moulding of Glass Mat Thermoplastics (GMT), Int. J. Mater. Form. 1 (2008) 929–932.

[40] L. Orgéas, P.J.J. Dumont, S. Le Corre, Rheology of highly concentrated fiber suspensions, in: F. Ch inesta, G. Ausias (Eds.), Chapter in Rheology of Non-Spherical Particle Suspensions, ISTE Press, Elsevier 2015, pp. 119–168 (ISBN: 9781785480362).

[41] P. Dumont, L. Orgéas, D. Favier, P. Pizette, C. Venet, Compression moulding of SMC: in situ experiments modelling and simulation, Compos. Part Appl. S. A 38 (2007) 353–368.

[42] R.M. Bowen, Continuum Physics III: Mixtures and EM Field Theories, vol. III, Academic Press, 1976.

[43] P. Dumont, S. Le Corre, L. Orgéas, D. Favier, C. Gaborit, P. Lory, Finite element implementation of a two-phase model for compression molding of composites, Eur. Finite Elem. Rev. 14 (2005) 883–900.

[44] S. Toll, Note: on the tube model for fiber suspensions, J. Rheol. 37 (1) (1993) 123–125.

[45] O. Guiraud, L. Orgéas, P.J.J. Dumont, S. Rolland du Roscoat, Microstructure and deformation micro-mechanisms of concentrated fiber bundle suspensions: an analysis combining X-ray microtomograpy and pull-out tests, J. Rheol. 56 (3) (2012) 593–623.

[46] O. Guiraud, P.J.J. Dumont, L. Orgéas, D. Favier, Rheometry of compression moulded fiber-reinforced polymer composites: rheology, compressibility, and friction forces with mould surfaces, Compos. Part A Appl. S. A 43 (2012) 2107–2121.

[47] L. Orgéas, P.J.J. Dumont, J.-P. Vassal, O. Guiraud, V. Michaud, D. Favier, In-plane conduction of polymer composite plates reinforced with architectured copper fibers, J. Mater. Sci. 47 (2012) 2932–2942.

[48] E. Sanchez-Palencia, Nonhomogeneous media and vibration theory, Lecture Note in Physics 127, Springer Verlag, Berlin, 1980.

[49] J.-L Auriault, Heterogeneous medium, Is an equivalent macroscopic description possible? Int. J. Eng. Sci. 29 (7) (1991) 785–795.

[50] C. Boutin, Study of permeability by periodic and self-consistent homogenisation, Eur. J. Mech. A. Solids 19 (4) (2000) 603–632.

[51] Z. Idris, L. Orgéas, C. Geindreau, J.-F. Bloch, J.-L. Auriault, Microstructural effects on the flow law of power-law fluids through fibrous media, Model. Simul. Mater. Sci. 12 (5) (2004) 995–1015.

[52] S. Rolland du Roscoat, M. Decain, C. Geindreau, X. Thibault, J.-F. Bloch, Microstructural analysis of paper using synchrotron X-ray microtomography: numerical estimation of the permeability and effective thermal conductivity, Appita J. 61 (4) (2008) 286–290.

[53] V. Koivu, M. Decain, C. Geindreau, K. Mattila, J.-F. Bloch, M. Kataja, Transport properties of heterogeneous materials. Combining computerised X-ray micro-tomography and direct numerical simulations, Int. J. Comput. Fluid Dyn. 23 (10) (2009) 713–721.

[54] H. Darcy, Les fontaines publiques de la ville de Dijon, Victor Valmont, Paris, 1856.

[55] T. Kanit, S. Forest, I. Galliet, V. Mounoury, D. Jeulin, Determination of the size of the representative volume element for random composites: statistical and numerical approach, Int. J. Solids Struct. 40 (2003) 3647–3679.

[56] A. Perrot, T. Lecompte, H. Khelifi, C. Brumaud, J. Hot, N. Roussel, Yield stress and bleeding of fresh cement pastes, Cem. Concr. Compos. 42 (2012) 937–944.

[57] A. Perrot, D. Rangeard, V. Picandet, Y. Mélinge, Hydro-mechanical properties of fresh cement pastes containing polycarboxylate superplasticizer, Cem. Concr. Compos. 53 (2013) 221–228.

[58] H. Khelifi, A. Perrot, T. Lecompte, D. Rangeard, G. Ausias, Prediction of extrusion load and liquid phase filtration during ram extrusion of high solid fraction pastes, Powder Technol. 249 (2013) 258–268.

[59] F. Loix, P. Badel, L. Orgéas, C. Geindreau, P. Boisse, Woven fabric permeability: from textile deformation to fluid flow mesoscale simulations, Compos. Sci. Technol. 68 (2008) 1624–1630.

[60] N. Calonne, C. Geindreau, F. Flin, S. Morin, B. Lesaffre, S. Rolland du Roscoat, P. Charrier, 3-D image-based numerical computations of snow permeability: links to specific surface area, density, and microstructural anisotropy, Cryosphere Discuss. 6 (2012) 1157–1180.